

Momentum-space Aharonov-Bohm interferometry in Rashba spin-orbit coupled Bose-Einstein condensates

Junpeng Hou, Xi-Wang Luo, Kuei Sun, and Chuanwei Zhang*

Department of Physics, The University of Texas at Dallas, Richardson, Texas 75080-3021, USA

Since the recent experimental realization of synthetic Rashba spin-orbit coupling paved a new avenue for exploring and engineering topological phases in ultracold atoms, a precise, solid detection of Berry phase has been desired for unequivocal characterization of system topology. Here, we propose a scheme to conduct momentum-space Aharonov-Bohm interferometry in a Rashba spin-orbit coupled Bose-Einstein condensate with a sudden change of in-plane Zeeman field, capable of measuring the Berry phase of Rashba energy bands. We find that the Berry phase with the presence of a Dirac point is directly revealed by a robust dark interference fringe, and that as a function of external Zeeman field is characterized by the contrast of fringes. We also build a variational model describing the interference process with semiclassical equations of motion of essential dynamical quantities, which lead to agreeable trajectories and geometric phases with the real-time simulation of Gross-Pitaevskii equation. Our study would provide timely guidance for the experimental detection of Berry phase in ultracold atomic systems and help further investigation on their interference dynamics in momentum space.

I. INTRODUCTION

Topological orders of matter have recently gained great attentions in solid-state and cold-atom physics [1–14], for their characterization of quantum phases in a different scenario from the conventional Ginzburg-Landau orders [15, 16] and potential application on fault-tolerant quantum computation [17–19]. A large variety of topological phases, including quantum Hall states [20–22], topological insulators [23, 24], and anomalous Hall states [25–27], can be characterized by a geometric phase [28], or Berry phase, of the underlying band structure of the system. In this context, direct measurement of Berry phase is essential for exploring the new physics of topological states of matter.

Following the definition of Berry phase, i.e., the adiabatic phase shift of wavefunction along a closed loop in parameter space, one could borrow an analogous idea for the detection of Berry phase from the Aharonov-Bohm interferometry [29], in which the interference between two charged particles encircling a magnetic flux measures the associated geometric phase in real space. Differently, the interferometry for detecting Berry phase on an energy band should be performed in momentum space. Although it is a big challenge to realize the electronic interferometry in solid-state systems, an Aharonov-Bohm interferometer in reciprocal (lattice-momentum) space has recently been realized with ultracold atoms in optical lattices and has successfully measured the Berry phase of two-dimensional (2D) hexagonal lattice systems [1, 30].

Ultracold atomic gases exhibit great flexibility and controllability in engineering exotic, on-demand single-particle energy bands of a spatially continuous system [31–43]. In particular, a distinct type of single-

particle band governed by 2D Rashba spin-orbit coupling [44–49] has been experimentally realized in both ultracold Fermi [50, 51] and Bose [52] gases. Since such a band structure can exhibit a Dirac point, from which crucial topological properties may emerge, probing its nontrivial Berry phase is hence among the first experimental pursuits after the initial realization in ultracold atoms.

In this paper, we propose a practical scheme that conducts momentum-space Aharonov-Bohm interferometry in Rashba spin-orbit coupled Bose-Einstein condensates (BECs), hence measuring the Berry phase along a loop enclosing the Dirac point. As shown in Fig. 1(a), our interferometer exploits the intrinsic ring structure in the Rashba energy band as the interferometer loop and the controllable detuning $\delta_x \sigma_x$ of ultracold atoms as a trigger

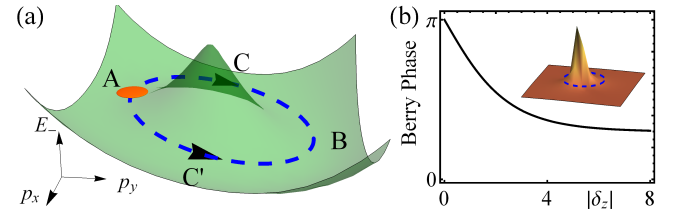


FIG. 1. (Color online) (a) Illustration of the momentum-space Aharonov-Bohm interferometry. A BEC (orange spot) with Rashba spin-orbit coupling is initially at the ground state A. After a sudden change of detuning δ_x , the deformation of energy spectrum $E_-(p_x, p_y)$ lifts point A, and then the BEC wavefunction packet splits into two, separately moving along paths C and C' and encountering each other at point B. The whole path encircles nonzero Berry flux localized around the tip of the shadow region (the Dirac point if $\delta_z = 0$), resulting in a Berry phase directly indicated by the interference pattern. (b) Berry phase versus detuning δ_z , which can be determined by experimentally measured interference pattern through the procedure in (a). The inset shows the schematic Berry curvature, mostly encircled by the ring path, in the p_x - p_y plane.

* Corresponding author.

Email: chuanwei.zhang@utdallas.edu

for driving the BEC. A sudden change of δ_x sets up the initial BEC state at the highest energy point of the ring (point A), and as the BEC naturally pursues the lowest energy (point B), it splits into two, following different halves of the ring (C and C') and exhibiting the interference. Since the whole ring path encloses region with dense Berry flux, the interference pattern would reflect the Berry phase as a function of δ_z , as in Fig. 1(b). At $\delta_z = 0$, the Berry phase equal to π indicates the presence of a Dirac point.

We adopt two complementary methods, Gross-Pitaevskii equation (GPE) simulation and variational analysis, for studying the BEC dynamics and interference. Our simulation shows real-time evolution of the interference pattern for ^{87}Rb BECs in typical cold-atom experiments, while the variational analysis provides an informative model capturing the key physical features of the interference, including the trajectories in momentum and real space as well as the geometric phase acquired during the evolution. We also point out proper conditions for external trapping potential and interatomic interaction under which the interferometry procedure succeeds and discuss why improper trapping frequency or too strong interaction sabotages the desired dynamics for the interference. Our results ought to provide timely guidance for ongoing experimental study on the Rashba spin-orbit coupled quantum gases.

In Sec. II, we present the model Hamiltonian and the associated Berry phase on its lowest energy band. In Sec. III, we discuss the detailed procedure for the momentum-space Aharonov-Bohm interferometry and its physical requirement. We then show real-time simulation results, which reveal the relation between interference fringe contrast and Berry phase. In Sec. IV, we propose a variational BEC wavefunction and derive its equation of motion, which characterizes trajectories of the two splitting wave packets as well as the accumulated geometric phase during the evolution. Finally, we make a conclusion in Sec. V.

II. MODEL AND HAMILTONIAN

We consider a Bose gas with atomic mass m and two hyperfine spin states $(\psi_\uparrow \ \psi_\downarrow)^T$ subject to synthetic Rashba coupling in x - y plane and tunable Zeeman field. After integrating out the irrelevant z degrees of freedom, we write down the effective Hamiltonian,

$$H = \frac{1}{2m}(\hat{p}_x^2 + \hat{p}_y^2) + V + H_R + H_Z + H_I, \quad (1)$$

with

$$V = \frac{m}{2}(\omega_x^2 \hat{x}^2 + \omega_y^2 \hat{y}^2), \quad (2)$$

$$H_R = \lambda_R(\hat{p}_y \sigma_x + a \hat{p}_x \sigma_y), \quad (3)$$

$$H_Z = \delta_x \sigma_x + \delta_z \sigma_z, \quad (4)$$

$$H_I = \begin{pmatrix} g_{\uparrow\uparrow}|\psi_\uparrow|^2 + g_{\uparrow\downarrow}|\psi_\downarrow|^2 & 0 \\ 0 & g_{\uparrow\downarrow}|\psi_\uparrow|^2 + g_{\downarrow\downarrow}|\psi_\downarrow|^2 \end{pmatrix}. \quad (5)$$

Here V is an external trapping potential, H_R describes the Rashba coupling of strength λ_R and anisotropy factor a , H_Z represents the Zeeman field δ_z (δ_x) in the longitudinal (transverse) direction (with the y component set to zero without loss of generality), and H_I results from the spin-dependent mean-field interaction, e.g., $g_{\uparrow\uparrow} = g_{\downarrow\downarrow} = 0.9554g_{\uparrow\downarrow} \equiv g$ in the following simulation for ^{87}Rb systems.

Given sufficiently weak trapping, the Hamiltonian has two single-particle energy bands in p_x - p_y momentum space, with the lower one being

$$E_- = \frac{\mathbf{p}^2}{2m} - |\vec{d}(\mathbf{p})|, \quad (6)$$

where $\mathbf{p} = (p_x, p_y)$ and $\vec{d} = (\lambda_R p_x + \delta_x, \lambda_R a p_y, \delta_z)$. At $a = 1$ and $\delta_x = 0$, the set of minima of E_- form a horizontal ring $|\mathbf{p}| = \sqrt{\lambda_R^4 - 4\delta_z^2}/(2\lambda_R)$ in the p_x - p_y plane. If $\delta_x \neq 0$, the ring structure remains but is inclined such that it has only one maximum and one minimum at the two intercepts with the p_y axis, respectively [as points A and B in Fig. 1(a)]. Our interferometry is performed along this Rashba ring path as we will show in Sec. III.

The Berry phase γ in the region enclosed by this ring loop can be computed as

$$\gamma = \oint_{L_c} \mathbf{A}_B \cdot d\mathbf{p} = \int_S \mathcal{F} d^2\mathbf{p}, \quad (7)$$

where $\mathbf{A}_B = -i\langle\zeta(\mathbf{p})|\nabla_{\mathbf{p}}|\zeta(\mathbf{p})\rangle$ is Berry connection corresponding to eigenstate $\zeta(\mathbf{p})$, $\mathcal{F} = \nabla \times \mathbf{A}_B$ is Berry curvature, and L_c and S denote the loop and the enclosed region, respectively. For our Hamiltonian, the Berry curvature is related to the unit vector $\hat{d} = \vec{d}/|\vec{d}|$ as

$$\mathcal{F} = \frac{1}{2}\epsilon_{ij}\hat{d} \cdot (\partial_i \hat{d} \times \partial_j \hat{d}), \quad (8)$$

where ϵ_{ij} is the antisymmetric permutation (Levi-Civita) symbol, and the Berry phase is equal to half the solid angle swept by \hat{d} in the loop integral. The Berry phase depends on both δ_z and δ_x but is insensitive to the latter given $\delta_x/\lambda_R \ll 1$. At $\delta_z = 0$, the Berry curvature is a delta function centered at the Dirac point $(p_x, p_y) = (0, 0)$, which gives a Berry phase $\gamma = \pi$. With δ_z increasing, the \hat{d} vector sweeps a less solid angle, and the Berry phase monotonically decreases as shown in Fig. 1(b). Therefore, one can continuously change the Berry phase by tuning δ_z , in analogy of changing the magnetic flux in a conventional Aharonov-Bohm interferometer.

III. INTERFEROMETRY AND SIMULATION

In this section, we discuss how to employ our model as an Aharonov-Bohm interferometer for detecting the Berry phase and present the GPE simulation results. In cold-atom systems, the Rashba spin-orbit coupling is generated by a set of Raman lasers that couple different spin

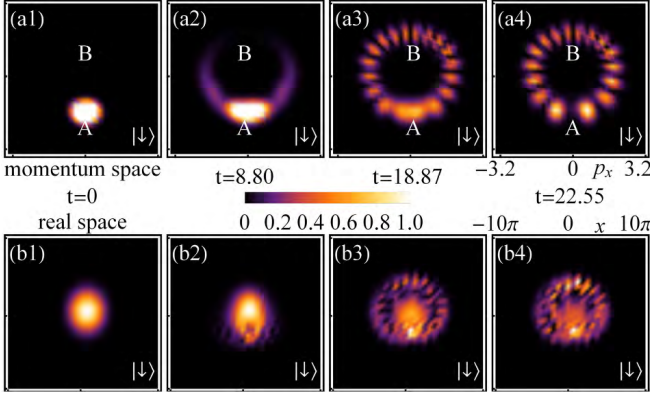


FIG. 2. (Color online) Time evolution (in units of ms) of down-spin density distribution in p_x - p_y (top) and x - y (bottom) planes from GPE simulation (the up-spin component exhibits same dynamics). (a1)-(a4) A ground-state BEC is first prepared at a band minimum A. After a change of δ_x at $t = 0$, it starts to split, travel along the ring path. An interference pattern can then be observed after the tails of wavefunctions meet at the other side of ring (point B). (b1)-(b4) Corresponding real-space density distributions. The parameters are set as $\lambda_R = 1.5$, $a = 1$, $\delta_z = 1$ kHz, $\delta_0 = -350$ Hz, $\delta_1 = 400$ Hz, and $ng = 0.05$.

and momentum states, and the Zeeman energy shift is determined by the relative detunings of the lasers [50–52]. All the parameters are highly tunable in the current experimental setup. We consider a trapped BEC initially prepared at the ground state of fixed λ_R , a , δ_z , and $\delta_x = \delta_0 < 0$, which is a momentum Gaussian wave packet (due to the trap) centered at the minimum of the inclined ring or $(0, -p_0)$. Then the detuning δ_x is suddenly changed to $\delta_x = \delta_1 > 0$ (with other parameters unchanged). The ring structure is hence inversely inclined, such that the current location of the condensate becomes the energy maximum [with a slight deviation $\sim O(\delta_x \delta_z^2)$, which is negligible in our case], illustrated as point A in Fig. 1(a). As a result, the BEC wavepacket will split into two, which follow separate paths (C and C', respectively) and move toward the new energy minimum at the opposite end of the ring (point B). As the two waves meet and superpose at point B, the dynamic phase cancels out due to the symmetry between the two paths, while the geometric phase (Berry phase), as a function of λ_R , a , δ_z , and $\delta_x = \delta_1$, can be revealed by the density contrast of the interference pattern.

We remark that a proper external trap is essential for driving the motion of the condensate in momentum space since $d\hat{p}/dt = i[H, \hat{p}] = i[V, \hat{p}] \neq 0$ (given the negligible interaction). If there is no trap, any \mathbf{p} state is a stationary state, so the BEC does not move. However, if the trapping potential is too strong (comparable to Rashba coupling strength), it may also spoil the desired ground state as well as the interference dynamics in our system [53, 54]. In addition, if the interaction is too strong, the initial BEC wavepacket spontaneously selects one path

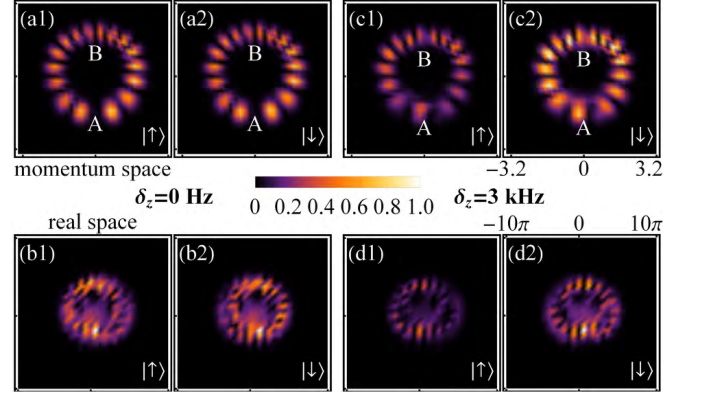


FIG. 3. (Color online) Momentum-space (top) and real-space (bottom) density distributions for each spins (as labeled on the bottom-right corner of each panel) from GPE simulation for $\delta_z = 0$ at $t = 23.44$ ms (left four panels) and $\delta_z = 3$ kHz at $t = 21.71$ ms (right four panels), with the other parameters the same as in Fig. 2. (a1) and (a2): at $\delta_z = 0$, there is a dark fringe (with zero density) at point B, reflecting a π Berry phase given by the Dirac point. (c1) and (c2): at $\delta_z = 3$ kHz, finite density occurs at point B as the Berry phase deviates significantly from π .

rather than splits into two parts. This is because the superposition of two momentum wavepackets leads to a real-space density wave that costs too much interaction energy. Furthermore, the Zeeman field δ_z cannot be too large. Otherwise the energy-band tip will be flattened, and consequently, the condensate will not follow the shallow Rashba ring groove.

Given the above constraints, our GPE simulation shows that typical experimental parameters are indeed suited for realizing the interference as shown in Fig. 2. In panels (a1)–(a4), we plot density distributions $\rho_{\downarrow}(\mathbf{p})$ in momentum space at different time frames, with the starting point on the ring path labeled by A and the pursued energy minimum by B. Initially, the condensate locates at A [(a1)], which is lifted from the ground state by the sudden change in δ_x . Then the BEC splits into two, which separately follow the ring loop [as C and C' in Fig. 1(a)] toward B [(a2)]. After the two parts encounter each other at point B, a clear ring-shape interference pattern forms in momentum-space [(a3, a4)]. Note that our simulation is preformed in the whole 2D plane without any constraint in coordinates (x, y, p_x, p_y) . This ring structure indeed reflects the BEC's natural motion along the ring groove toward the lower energy in the Rashba band. Due to this petal pattern in momentum space, the condensate also exhibits exotic circular distributions in real-space [(b1)–(b4)]. In Sec. IV, our variational analysis of key dynamical variables will show that the trajectories of splitting BEC's center of mass explain the pattern exhibited by the GPE simulation results in both momentum and real space.

Here, we turn to study the interference pattern at various Zeeman field δ_z . The GPE simulation results are pre-

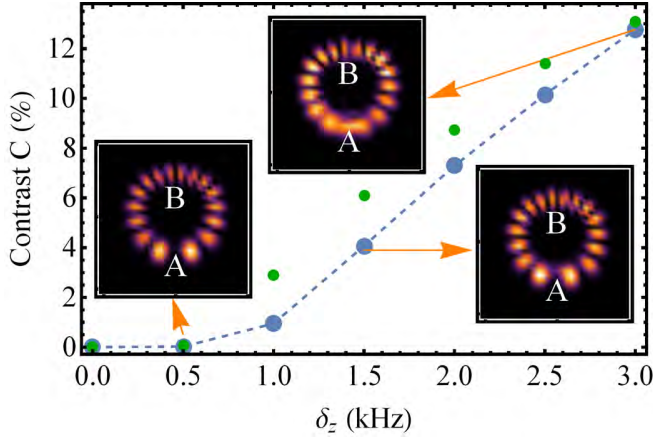


FIG. 4. (Color online) Fringe contrast C versus δ_z from the GPE simulation (blue) and variational analysis (green). Both show a monotonic increase in C as δ_z deviates away from 0. This monotonic behavior can be mapped to the monotonic trend of Berry phase vs δ_z in Fig. 1(b), such that C as a measurable can be used for directly determining the Berry phase. The insets show the momentum-space density distribution for the corresponding data points with different contrast. All the parameters except δ_z are the same as used in Fig. 2.

sented in Fig. 3. In panels (a1) and (a2), for $\delta_z = 0$, the density at point B is constantly zero during the evolution, forming a robust dark fringe that indicates a π phase shift between the splitting BECs upon the encounter at point B. Due to the aforementioned dynamic phase canceling, this π phase shift is contributed purely by the accumulated geometric phase around the loop, thus confirming the presence of a Dirac point. Panels (c1) and (c2) show a finite density at B for $\delta_z = 3$ kHz. This indicates the Berry phase no longer equal to π as we expect from the smaller solid angle swept by the \hat{d} vector. In Figs. 3 (b) and (d), we plot the corresponding real-space density distributions. They also exhibit a roughly ring-shape interference pattern and can be understood by considering the group velocity and phase dynamics of the wavepackets, as we will show in Sec. IV.

In order to quantitatively relate the interference pattern with the geometric phase, we define a local fringe contrast as

$$C = \frac{\int_{s_0} d\mathbf{p} \rho(\mathbf{p})}{\int_{s_n} d\mathbf{p} \rho(\mathbf{p})}, \quad (9)$$

where $\rho = \rho_{\uparrow} + \rho_{\downarrow}$ is the total density distribution in momentum space, s_0 is a proper dark-fringe region around point B, and $s_n \supset s_0$ includes the adjacent bright-fringe regions (such that $0 \leq C \leq 1$). While $C = 0$ all the time at $\delta_z = 0$, it becomes nonzero as the interference occurs for any $\delta_z > 0$. Note that since the contrast may slightly oscillates with time, in our simulation, we record C right after the center of masses of the left and right parts of BEC both move cross the p_x axis. In Fig. 4, we plot C vs δ_z obtained from the GPE simulation (blue

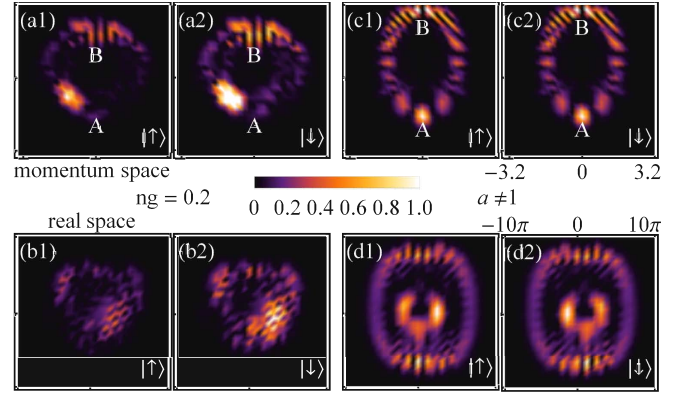


FIG. 5. (Color online) Momentum and real-space density distributions for large interaction $ng = 0.2$ (left four panels) and anisotropic Rashba coupling $a = 0.8$ (right four panels) from the GPE simulation. Convention is the same as Fig. 3. (a1) and (a2): the whole condensate spontaneously choose one side of the ring rather than split due to the interaction (at 15.41 ms). (c1) and (c2): a robust dark fringe still occurs at point B at anisotropic Rashba coupling, indicating that the π Berry phase is independent of the deformation in energy band and interference loop (at 32.32 ms). The parameter changes also affect the real-space density distribution in the bottom row. Our variational analysis confirms the same physics.

dots), which fit a monotonically increasing curve (dashed curve). Mapped onto the monotonically decreasing relation between Berry phase and δ_z , as in Fig. 1(b), this fringe contrast C may act as a good experimental measurable for directly determining the geometric phase of the energy band. As we will show in Sec. IV, a variational analysis for the interference dynamics also yields a comparable C - δ relation (green dots).

Finally, we study the effects of strong interaction and anisotropic Rashba coupling in the experiment. As mentioned above, a reasonably small interaction strength is favored for our scheme. If the interaction is too strong, splitting of BEC wavefunction in momentum space will induce real space density modulation that highly increase the interaction energy. Consequently, the condensate will spontaneously select one route rather than equally split. This is shown by the GPE simulation results in Fig. 5 (a1) and (a2), in which all the parameters are the same as those in Fig. 3(c,d) except $ng = 0.2$ is quadrupled. We see that the axial symmetry is broken in both momentum and real space, and the interference fringes become more obscure. In experiments, the Rashba coupling can be anisotropically tuned, i.e., $a \neq 1$ in Eq. (3). As a result, the ring structure of the energy band becomes elliptical, so does the interference loop. In the right four panels of Fig. 5, we show the GPE simulation results for $a = 0.8$, with the other parameters same as Fig. 3(a,b). We still see a dark interference fringe with zero density at point B, indicating the π Berry phase robust against the deformation of energy band and interference loop, as expected for the property of Dirac point.

IV. VARIATIONAL ANALYSIS

In this section, we reveal salient physical features of the dynamical interference process with a simply structured variational wave function. Since we have observed in the GPE simulation that the BEC wavefunction intends to split into two under weak interatomic interactions, it is natural to consider a superposition that can describe the splitting condensate, as

$$\Psi_{\text{var}} = \phi_L e^{i\frac{\varphi}{2}} \cos \alpha + \phi_R e^{-i\frac{\varphi}{2}} \sin \alpha, \quad (10)$$

which consists of two Gaussian wavepackets $\phi_{j=R,L}$ in the region of $p_x > 0$ and $p_x < 0$, respectively. Each Gaussian wavepacket takes a general form [55, 56] as

$$\phi_j = \zeta(\mathbf{p}_j) \prod_{\eta} \left[\left(\frac{2}{\pi R_{\eta}^2} \right)^{\frac{1}{4}} e^{-\left(\frac{1}{R_{\eta}^2} - \frac{i}{2} \xi_{\eta} \right) (r_{\eta} - A_{j,\eta})^2} \times e^{ip_{j,\eta}(r_{\eta} - A_{j,\eta})} \right], \quad (11)$$

where $\eta = x, y$ stands for the spatial coordinates, A_{η} is the center of mass position (in real space), R_{η} is the width of the wavepacket, and ξ_{η} is introduced as the conjugate variable for R_{η} , which is essential for the completeness of this variational method [56]. The axial symmetry of the dynamics allows us to assume that the two wavepackets have the same R_{η} and ξ_{η} (independent of $j = L, R$), which have also been confirmed by our GPE simulation given reasonably weak interaction. In a semiclassical picture, the system Lagrangian $\mathcal{L} = \int d^2\mathbf{r} \Psi^{\dagger} (i \frac{\partial}{\partial t} - H) \Psi$ derives the equations of motions (see details in Appendix A) as

$$\frac{d}{dt} A_{j,\eta} = \frac{\partial}{\partial p_{j,\eta}} E_{j,-}, \quad \frac{d}{dt} p_{j,\eta} = -\omega_{\eta}^2 A_{j,\eta}, \quad (12)$$

$$\frac{d}{dt} \xi_{\eta} = \frac{4}{R_{\eta}^4} - \omega_{\eta}^2 - \xi_{\eta}^2, \quad \frac{d}{dt} R_{\eta} = R_{\eta} \xi_{\eta}, \quad (13)$$

with $\alpha = \alpha_0$ being time-independent and

$$\begin{aligned} \frac{d\varphi}{dt} = & \frac{1}{2} \left(\frac{\partial E_{L,-}}{\partial \alpha} \cot \alpha - \frac{\partial E_{R,-}}{\partial \alpha} \tan \alpha \right) \\ & + \sum_{j,\eta} \epsilon_j \left(p_{j,\eta} \frac{dA_{j,\eta}}{dt} - \frac{1}{2} \omega_{\eta}^2 A_{j,\eta}^2 - E_{j,-} \right. \\ & \left. - i \langle \zeta(\mathbf{p}) | \partial_{\mathbf{p}_{\eta}} \zeta(\mathbf{p}) \rangle \frac{dp_{\eta}}{dt} \Big|_{p_{\eta}=p_{j,\eta}} \right), \end{aligned} \quad (14)$$

where $E_{j,-} = E_{-}(\mathbf{p}_j)$ and $\epsilon_{j=L,R} = \pm 1$.

We choose the initial condition (at $t = 0$) of Eq. (12) as $A_x = A_y = 0$ for both wavepackets (same starting point) and small $p_{L,x} = -p_{R,x}$ for the initial velocity under slight axisymmetric perturbation in momentum space. Such symmetry is actually preserved by the equations of motion. The initial condition for Eq. (13) is obtained from the minimization of system energy functional. The trajectories generated by those equations are presented in Fig. 6, in good agreement with the GPE results in Fig. 3. Note that we also assume the equal splitting of

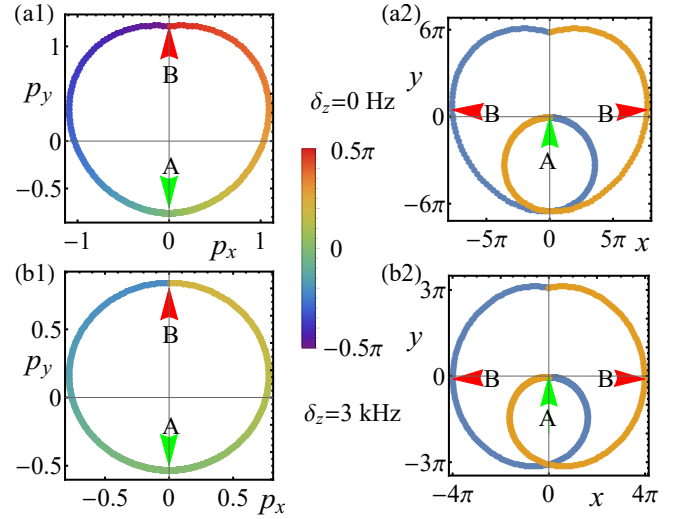


FIG. 6. (Color online) Center-of-mass trajectories of the two variational wavepackets in Eq. (10) in momentum space (left) and real space (right). In momentum space, the two trajectories accumulate a relative phase (represented by colors in bar graph) from 0 at point A to π at point B. In real space, the two trajectories (blue and orange curves, respectively) form a double-circle structure, with points A and B indicating the corresponding positions in momentum space. (a1,a2) [(b1,b2)] are for $\delta_z = 0$ Hz (3 kHz). The trajectories are comparable to the GPE simulation results in Fig. 3.

condensate, or $\alpha = \pi/4$, given sufficiently weak interaction.

We turn to discuss the dynamics of phase φ of the variational wave function. There are three different contributions to the time derivative of φ —the first comes from energy terms $E_{j,-}$, the second is related to the dynamic parameters like center-of-mass position and momentum, and the last is just the Berry connection \mathbf{A}_B , determined together by the spinor wavefunction and time derivative of momentum. Note that with the axial symmetry to the y (and p_y) axis, all the terms related to energy and other dynamical parameters, such as A_j^2 and p_j , vanish, leaving only the last term on the RHS of Eq. (14), which becomes

$$\frac{d}{dt} \varphi = -i \sum_{j,\eta} \epsilon_j \left(\langle \zeta(\mathbf{p}) | \partial_{\mathbf{p}_{\eta}} \zeta(\mathbf{p}) \rangle \frac{dp_{\eta}}{dt} \Big|_{p_{\eta}=p_{j,\eta}} \right). \quad (15)$$

This is exactly the Berry phase defined on the ring loop since

$$\oint_{L_c} \mathbf{A}_B \cdot d\mathbf{p} = \oint_{L+R} \mathbf{A}_B \cdot d\mathbf{p} = - \oint_L \mathbf{A}_B \cdot d\mathbf{p} + \oint_R \mathbf{A}_B \cdot d\mathbf{p}, \quad (16)$$

where the ring-shape loop L_c is divided into two parts L_j , as for each part of the splitting condensate. The integral direction of left hand side (L) is clockwise, hence carrying a minus sign. The numerical solutions of φ are illustrated in Fig. 6 (a1) and (b1) as the curve color. In panel (a1), the two wavepackets acquires an opposite

geometric phase as they encircle the loop. When they encounter each other at point B, the accumulated phases are $\pm\frac{\pi}{2}$, respectively, making a π phase difference, which results in a dark fringe. However, with an extra Zeeman field δ_z , such phase difference never reaches π at point B [(a2)]. The contrast C defined in Eq. (9) is also evaluated by the variation analysis, and the results (green dots) are compared with those from GPE (blue dots) in Fig. 4. They indeed show the same monotonic trend.

We remark that the variational method well captures the physical features of the interference dynamics as well as the geometric phase with much fewer variables than the GPE simulation. Solving the semiclassical equations of motion is also computationally efficient compared with the GPE simulation. Such an analysis is particularly useful for first searching a wide parameter region for exotic physics, then followed by further confirmation with the GPE simulation.

V. CONCLUSION

We have proposed and investigated a realistic approach for conducting momentum-space Aharonov-Bohm interferometry in Rashba spin-orbit coupled Bose gases and shown that the interference pattern measures the Berry phase of Rashba energy band. Our approach utilizes the ring structure of Rashba spectrum as the interferometry loop and the ultracold atoms tunability for triggering the motion of BEC wavepackets along the loop. With

the real-time GPE simulation for realistic ^{87}Rb gases, we have found that the density contrast of the interference fringes directly indicates the Berry phase as a monotonic function of Zeeman detuning. In particular, the π Berry phase of a Dirac point (without the detuning) is exhibited by a robust dark fringe (or zero contrast) at the end of interferometry loop. Additionally, we have modeled the interference dynamics with a variational wavefunction of splitting wavepackets and derived semiclassical equations of motion for the most relevant dynamical factors. The variational results have confirmed the trajectories in both momentum and real space as well as the local geometric phase acquired by the condensate along the momentum trajectory. The complementary variational analysis and GPE simulation well agree with each other.

Our study would provide guidance for ongoing experimental effort measuring the Berry phase in ultracold atoms with synthetic Rashba spin-orbit coupling. The simulated density pattern in momentum and real space (Figs. 2, 3, and 5) can be directly compared with the time-of-flight and direct-imaging measurements, respectively, in the experiment of ^{87}Rb gases. Our analysis can be extended to different experimental conditions such as an anisotropic ring loop or a loop with several local minima. The interferometry approach may find wide applications on various nontrivial energy bands as well as on high-spin [57–63] systems.

Acknowledgements. This work is supported by AFOSR (FA9550-16-1-0387), NSF (PHY-1505496), and ARO (W911NF-17-1-0128).

Appendix A: Semiclassical Equation of motion

We start from a single wavepacket and study its dynamics through deriving the semiclassical equation of motion. We assume that the Zeeman field is relatively weak and the barrier at the center of the Rashba ring is not flattened so that the condensate follows the band minimum in lower band. The normalized wavefunction ansatz can be written as

$$\phi = \zeta(\mathbf{p}) \prod_{\eta=x,y} \left(\frac{2}{\pi R_\eta^2} \right)^{\frac{1}{4}} e^{-(\frac{1}{R_\eta^2} - \frac{i}{2}\xi_\eta)(r_\eta - A_\eta)^2} e^{ip_\eta(r_\eta - A_\eta)} \quad (\text{A1})$$

where A_η is the center-of-mass position, R_η is the width of the wavepacket, ξ_η is the conjugate variable for R_η and $\zeta(\mathbf{p})$ is normalized spin wave function taken as the lowest eigenstate of H_0 . Now, we can compute the energy functional

$$E = E_- + \sum_{\eta=x,y} \left(\frac{1}{2R_\eta^2} + \frac{1}{8}\xi_\eta^2 R_\eta^2 + \frac{1}{2}\omega_\eta^2 \left(A_\eta^2 + \frac{1}{4}R_\eta^2 \right) \right). \quad (\text{A2})$$

Note that we have ignored the interaction term at this momentum since it plays no important role in the dynamics (we also require this to be a weakly interacting system) and E_- is the eigenvalue of single particle Hamiltonian H_0 . The system Lagrangian is defined as $\mathcal{L} = \int d^2\mathbf{r} \phi^* (i\frac{\partial}{\partial t} - H)\phi$, that is

$$\mathcal{L} = \sum_{\eta} \left(p_\eta \frac{d}{dt} A_\eta - \frac{R_\eta^2}{8} \frac{d}{dt} \xi_\eta + i\langle \zeta(\mathbf{p}) | \partial_{p_\eta} \zeta(\mathbf{p}) \rangle \frac{d}{dt} p_\eta \right) - E, \quad (\text{A3})$$

and correspondingly, EoMs are given by Lagrangian equations

$$\frac{d}{dt} A_\eta = \frac{\partial}{\partial p_\eta} E_-, \quad \frac{d}{dt} p_\eta = -\omega_\eta^2 A_\eta; \quad (\text{A4})$$

$$\frac{d}{dt}\xi_\eta = \frac{4}{R_\eta^4} - \omega_\eta^2 - \xi_\eta^2, \quad \frac{d}{dt}R_\eta = R_\eta\xi_\eta.$$

Notice that, the term $i\langle\zeta(\mathbf{p})|\partial_{p_\eta}\zeta(\mathbf{p})\rangle\frac{d}{dt}p_\eta$ does not have any contribution to the dynamics in our case, indicating it may relate to Berry phase, which is already demonstrated in the main text. Meanwhile, EoMs for the conjugate pair (A_η, p_η) are the same if one takes E_- as the Hamiltonian and applies Hamiltonian formalisms directly.

So far, the EoMs we got only concerns about a single dipole motion, and thus, it is suitable to describe the oscillation or other motion when BEC does not split into two parts (or more).

To study the Berry phase, we must have two individual wavepacket interferences with each other. We presume that the condensate will split into two parts ϕ_L (left) and ϕ_R (right). As they continue to move on the ring, they will overlap at some point. In this case, the wavefunction of the whole condensate can be written as

$$\Psi_c = \Psi_L + \Psi_R = \phi_L e^{i\frac{\varphi}{2}} \cos \alpha + \phi_R e^{-i\frac{\varphi}{2}} \sin \alpha, \quad (\text{A5})$$

where we use subscript c to denote a physical quantity when it combines both side (L and R) together and $\phi_j, j = L, R$ is defined as

$$\phi_j = \zeta(\mathbf{p}_j) \prod_\eta \left(\frac{2}{\pi R_\eta^2} \right)^{\frac{1}{4}} e^{-(\frac{1}{R_\eta^2} - \frac{i}{2}\xi_\eta)(r_\eta - A_{j,\eta})^2} e^{ip_{j,\eta}(r_\eta - A_{j,\eta})}, \quad (\text{A6})$$

as the two wavepackets suppose to share the same conjugate variables (R_η, ξ_η) . Typically, we have $\omega_\eta \ll \Omega$ so that the translation symmetry is still keeping and $\mathbf{R} \cdot (\mathbf{p}_L - \mathbf{p}_R) \gg 1$. With this approximation, the overall energy functional is just the summation of that of two wavepackets

$$E_c = E_{L,-} \cos^2 \alpha + E_{R,-} \sin^2 \alpha + \sum_{\eta=x,y} \left(\frac{1}{2R_\eta^2} + \frac{1}{8}\xi_\eta^2 R_\eta^2 + \frac{1}{8}\omega_\eta^2 R_\eta^2 + \frac{1}{2}\omega_\eta^2 (A_{L,\eta}^2 \cos^2 \alpha + A_{R,\eta}^2 \sin^2 \alpha) \right), \quad (\text{A7})$$

where we denote $E_{j,-} = E_-(\mathbf{p}_j)$ and this further gives the Lagrangian

$$\begin{aligned} \mathcal{L}_c = & \sum_\eta \left(p_{L,\eta} \frac{dA_{L,\eta}}{dt} \cos^2 \alpha + p_{R,\eta} \frac{dA_{R,\eta}}{dt} \sin^2 \alpha - \frac{R_\eta^2}{8} \frac{d}{dt} \xi_\eta \right) - \frac{1}{2} \frac{d\varphi}{dt} \cos 2\alpha - E_c \\ & + i \sum_\eta \left(\langle\zeta(\mathbf{p})|\partial_{\mathbf{p}_\eta}\zeta(\mathbf{p})\rangle \frac{dp_\eta}{dt} \Big|_{p_\eta=p_{L,\eta}} \cos^2 \alpha + \langle\zeta(\mathbf{p})|\partial_{\mathbf{p}_\eta}\zeta(\mathbf{p})\rangle \frac{dp_\eta}{dt} \Big|_{p_\eta=p_{R,\eta}} \sin^2 \alpha \right). \end{aligned} \quad (\text{A8})$$

Before proceeding to derive the equations of motion, notice that \mathcal{L}_c is independent of φ and only has one term $-\frac{1}{2}\frac{d\varphi}{dt} \cos 2\alpha$ containing the time derivative of φ , indicating α is a constant. This can simplify the EoMs significantly. Applying Lagrangian equations, one may find that the dynamics of classical momentum and position (center of mass) for left and right side are independent of each other. Moreover, R_η and ξ_η still follow the same equation as before. So, the essential part is the relative phase φ , which is govern by

$$\begin{aligned} \frac{d\varphi}{dt} = & \frac{1}{2} \left(\frac{\partial E_{L,-}}{\partial \alpha} \cot \alpha - \frac{\partial E_{R,-}}{\partial \alpha} \tan \alpha \right) - (E_{L,-} - E_{R,-}) \\ & + (p_{L,\eta} \frac{dA_{L,\eta}}{dt} - p_{R,\eta} \frac{dA_{R,\eta}}{dt}) - \frac{1}{2}\omega_\eta^2 (A_{L,\eta}^2 - A_{R,\eta}^2) \\ & - i \sum_\eta \left(\langle\zeta(\mathbf{p})|\partial_{\mathbf{p}_\eta}\zeta(\mathbf{p})\rangle \frac{dp_\eta}{dt} \Big|_{p_\eta=p_{L,\eta}} - \langle\zeta(\mathbf{p})|\partial_{\mathbf{p}_\eta}\zeta(\mathbf{p})\rangle \frac{dp_\eta}{dt} \Big|_{p_\eta=p_{R,\eta}} \right). \end{aligned} \quad (\text{A9})$$

Accounting for the interaction, one simply adds one more term in the energy functional,

$$f_g = \frac{1}{\sqrt{\pi}R_x R_y} \int d^2\mathbf{r} \left(g_0 |\Psi_c|^4 + g_2 |\Psi_c^* \mathbf{S} \Psi_c|^2 \right). \quad (\text{A10})$$

However, the interaction does not affect the Berry phase here, though it may cause a non-zero dynamic phase. Meanwhile, to avoid interaction-induced spontaneous symmetry break, which forces the condensate pick up one side, we require the system to have a small interaction strength.

- [2] L. Tarruell, D. Greif, T. Uehlinger, G. Jotzu & T. Esslinger, Creating, moving and merging Dirac points with a Fermi gas in a tunable honeycomb lattice, *Nature* **483**, 302 (2012).
- [3] P. Soltan-Panahi, J. Struck, P. Hauke, A. Bick, W. Plenkers, G. Meineke, C. Becker, P. Windpassinger, M. Lewenstein & K. Sengstock, Multi-component quantum gases in spin-dependent hexagonal lattices, *Nat. Phys.* **7**, 434 (2011).
- [4] M. Aidelsburger, M. Atala, S. Nascimbene, S. Trotzky, Y.-A. Chen, and I. Bloch, Experimental Realization of Strong Effective Magnetic Fields in an Optical Lattice, *Phys. Rev. Lett.* **107**, 255301 (2011).
- [5] L. W. Cheuk, A. T. Sommer, Z. Hadzibabic, T. Yefsah, W. S. Bakr, and M. W. Zwierlein, Spin-Injection Spectroscopy of a Spin-Orbit Coupled Fermi Gas, *Phys. Rev. Lett.* **109**, 095302 (2012).
- [6] F. Alex An, E. J. Meier and B. Gadway, Direct observation of chiral currents and magnetic reflection in atomic flux lattices, *Sci. Adv.* **3**, e1602685 (2017).
- [7] A. Celi, P. Massignan, J. Ruseckas, N. Goldman, I. B. Spielman, G. Juzeliūnas, and M. Lewenstein, Synthetic Gauge Fields in Synthetic Dimensions, *Phys. Rev. Lett.* **112**, 043001 (2014).
- [8] N. R. Cooper, Optical Flux Lattices for Ultracold Atomic Gases, *Phys. Rev. Lett.* **106**, 175301 (2011).
- [9] L.-K. Lim, C. M. Smith, and A. Hemmerich, Staggered-Vortex Superfluid of Ultracold Bosons in an Optical Lattice, *Phys. Rev. Lett.* **100**, 130402 (2008).
- [10] K. Osterloh, M. Baig, L. Santos, P. Zoller, and M. Lewenstein, Cold Atoms in Non-Abelian Gauge Potentials: From the Hofstadter “Moth” to Lattice Gauge Theory, *Phys. Rev. Lett.* **95**, 010403 (2005).
- [11] L. Fidkowski, X. Chen, and A. Vishwanath, Non-Abelian Topological Order on the Surface of a 3D Topological Superconductor from an Exactly Solved Model, *Phys. Rev. X* **3**, 041016 (2013).
- [12] X. Chen, F. J. Burnell, A. Vishwanath, and L. Fidkowski, Anomalous Symmetry Fractionalization and Surface Topological Order, *Phys. Rev. X* **5**, 041013 (2015).
- [13] J. Maciejko, V. Chua, and G. A. Fiete, Topological Order in a Correlated Three-Dimensional Topological Insulator, *Phys. Rev. Lett.* **112**, 016404 (2013).
- [14] M. Levin and X.-G. Wen, Detecting Topological Order in a Ground State Wave Function, *Phys. Rev. Lett.* **96**, 110405 (2006).
- [15] P. C. Hohenberg and A. P. Krehov, An introduction to the Ginzburg-Landau theory of phase transitions and nonequilibrium patterns, *Phys. Rep.* **572**, 1 (2015).
- [16] N. Read, Order Parameter and Ginzburg-Landau Theory for the Fractional Quantum Hall Effect, *Phys. Rev. Lett.* **62**, 86 (1989).
- [17] A. Y. Kitaev, Fault-tolerant quantum computation by anyons, *Ann. Phys.* **303**, 2 (2003).
- [18] C. Nayak, S. H. Simon, A. Stern, M. Freedman, and S. D. Sarma, Non-Abelian anyons and topological quantum computation, *Rev. Mod. Phys.* **80**, 1083 (2008).
- [19] J. D. Sau, R. M. Lutchyn, S. Tewari, and S. D. Sarma, Generic New Platform for Topological Quantum Computation Using Semiconductor Heterostructures, *Phys. Rev. Lett.* **104**, 040502 (2010).
- [20] D. Xiao, M.-C. Chang, and Q. Niu, Berry phase effects on electronic properties, *Rev. Mod. Phys.* **82**, 1959 (2010).
- [21] Y. Zhang, Y.-W. Tan, H. L. Stormer, & P. Kim, Experimental observation of the quantum Hall effect and Berry’s phase in graphene, *Nat. Phys.* **438**, 201 (2005).
- [22] D. J. Thouless, M. Kohmoto, M. P. Nightingale, and M. den Nijs, Quantized Hall Conductance in a Two-Dimensional Periodic Potential, *Phys. Rev. Lett.* **49**, 450 (1982).
- [23] X.-L. Qi and S.-C. Zhang, Topological insulators and superconductors, *Rev. Mod. Phys.* **83**, 1057 (2011).
- [24] M. Z. Hasan and C. L. Kane, Colloquium: Topological insulators, *Rev. Mod. Phys.* **82**, 3045 (2010).
- [25] N. Nagaosa, J. Sinova, S. Onoda, A. H. MacDonald, and N. P. Ong, Anomalous Hall effect, *Rev. Mod. Phys.* **82**, 1939 (2010).
- [26] F. D. M. Haldane, Berry Curvature on the Fermi Surface: Anomalous Hall Effect as a Topological Fermi-Liquid Property, *Phys. Rev. Lett.* **93**, 206602 (2004).
- [27] T. Jungwirth, Q. Niu, and A. H. MacDonald, Anomalous Hall Effect in Ferromagnetic Semiconductors, *Phys. Rev. Lett.* **88**, 207208 (2002).
- [28] M. V. Berry, F. R. S., Quantal phase factors accompanying adiabatic changes, *Proc. Royal Soc. A* **392**, 1802 (1984).
- [29] Y. Aharonov and D. Bohm, Significance of Electromagnetic Potentials in the Quantum Theory, *Phys. Rev.* **115**, 485 (1959).
- [30] A. H. Castro Neto, F. Guinea, N. M. R. Peres, K. S. Novoselov, and A. K. Geim, The electronic properties of graphene, *Rev. Mod. Phys.* **81**, 109 (2009).
- [31] Y.-J. Lin, K. Jiménez-García, and I. B. Spielman, Spin-orbit-coupled Bose-Einstein condensates, *Nature (London)* **471**, 83 (2011).
- [32] P. Wang, Z.-Q. Yu, Z. Fu, J. Miao, L. Huang, S. Chai, H. Zhai, and J. Zhang, Spin-Orbit Coupled Degenerate Fermi Gases, *Phys. Rev. Lett.* **109**, 095301 (2012).
- [33] C. Qu, C. Hamner, M. Gong, C. Zhang, and P. Engels, Observation of Zitterbewegung in a spin-orbit-coupled Bose-Einstein condensate, *Phys. Rev. A* **88**, 021604(R) (2013).
- [34] J.-R. Li, J. Lee, W. Huang, S. Burchesky, B. Shteynas, F. Ç. Top, A. O. Jamison, and W. Ketterle, A stripe phase with supersolid properties in spin-orbit-coupled Bose-Einstein condensates, *Nature (London)* **543**, 91 (2017).
- [35] M. A. Khamsehchi, K. Hossain, M. E. Mossman, Y. Zhang, T. Busch, M. M. Forbes, and P. Engels, Negative-Mass Hydrodynamics in a Spin-Orbit Coupled Bose-Einstein Condensate, *Phys. Rev. Lett.* **118**, 155301 (2017).
- [36] C. Qu, Z. Zheng, M. Gong, Y. Xu, Li Mao, X. Zou, G. Guo, and C. Zhang, Topological superfluids with finite-momentum pairing and Majorana fermions, *Nat. Commun.* **4**, 2710 (2013).
- [37] W. Zhang and W. Yi, Topological Fulde-Ferrell-Larkin-Ovchinnikov states in spin-orbit-coupled Fermi gases, *Nat. Commun.* **4**, 2711 (2013).
- [38] H. Zhai, Degenerate quantum gases with spin-orbit coupling: a review, *Rep. Prog. Phys.* **78**, 026001 (2015).
- [39] K. Sun, C. Qu, and C. Zhang, Spin-orbital-angular-momentum coupling in Bose-Einstein condensates, *Phys. Rev. A* **91**, 063627 (2015).
- [40] M. Demarco, and H. Pu, Angular spin-orbit coupling in cold atoms, *Phys. Rev. A* **91**, 033630 (2015).
- [41] C. Qu, K. Sun, and C. Zhang, Quantum phases of Bose-Einstein condensates with synthetic spin-orbital-angular-momentum coupling, *Phys. Rev. A* **91**, 053630 (2015).

- (2015).
- [42] Y. Xu, F. Zhang, and C. Zhang, Structured Weyl Points in Spin-Orbit Coupled Fermionic Superfluids, *Phys. Rev. Lett.* **115**, 265304 (2015).
 - [43] J. Hou, H. Hu, K. Sun, and C. Zhang, Super-quasicrystal in a Bose-Einstein condensate, [arXiv:1708.08898](#).
 - [44] H. Hu, L. Jiang, X.-J. Liu, and H. Pu, Probing Anisotropic Superfluidity in Atomic Fermi Gases with Rashba Spin-Orbit Coupling, *Phys. Rev. Lett.* **107**, 195304 (2011).
 - [45] T. Ozawa and G. Baym, Stability of Ultracold Atomic Bose Condensates with Rashba Spin-Orbit Coupling against Quantum and Thermal Fluctuations, *Phys. Rev. Lett.* **109**, 025301 (2012).
 - [46] S. Gopalakrishnan, I. Martin, and E. A. Demler, Quantum Quasicrystals of Spin-Orbit-Coupled Dipolar Bosons, *Phys. Rev. Lett.* **111**, 185304 (2013).
 - [47] B. M. Anderson, I. B. Spielman, and G. Juzeliūnas, Magnetically Generated Spin-Orbit Coupling for Ultracold Atoms, *Phys. Rev. Lett.* **111**, 125301 (2013).
 - [48] Z. F. Xu and L. You, Dynamical generation of arbitrary spin-orbit couplings for neutral atoms, *Phys. Rev. A* **85**, 043605 (2012).
 - [49] A. M. Dudarev, R. B. Diener, I. Carusotto, and Q. Niu, Spin-Orbit Coupling and Berry Phase with Ultracold Atoms in 2D Optical Lattices, *Phys. Rev. Lett.* **92**, 153005 (2004).
 - [50] L. Huang, Z. Meng, P. Wang, P. Peng, S.-L. Zhang, L. Chen, D. Li, Q. Zhou & J. Zhang, Experimental realization of two-dimensional synthetic spin-orbit coupling in ultracold Fermi gases, *Nat. Phys.* **12**, 540-544 (2016).
 - [51] Z. Meng, L. Huang, P. Peng, D. Li, L. Chen, Y. Xu, C. Zhang, P. Wang, and J. Zhang, Experimental Observation of a Topological Band Gap Opening in Ultracold Fermi Gases with Two-Dimensional Spin-Orbit Coupling, *Phys. Rev. Lett.* **117**, 235304 (2016).
 - [52] Z. Wu, L. Zhang, W. Sun, X.-T. Xu, B.-Z. Wang, S.-C. Ji, Y. Deng, S. Chen, X.-J. Liu, J.-W. Pan, Realization of two-dimensional spin-orbit coupling for Bose-Einstein condensates, *Science* **354**, 83 (2016).
 - [53] H. Hu, B. Ramachandhran, H. Pu, and X.-J. Liu, Spin-Orbit Coupled Weakly Interacting Bose-Einstein Condensates in Harmonic Traps, *Phys. Rev. Lett.* **108**, 010402 (2012).
 - [54] S. Sinha, R. Nath, and L. Santos, Trapped Two-Dimensional Condensates with Synthetic Spin-Orbit Coupling, *Phys. Rev. Lett.* **107**, 270401 (2011).
 - [55] Z. Chen and H. Zhai, Collective-mode dynamics in a spin-orbit-coupled Bose-Einstein condensate, *Phys. Rev. A* **86**, 041604(R) (2012).
 - [56] V. M. Pérez-García, H. Michinel, J. I. Cirac, M. Lewenstein, and P. Zoller, Low Energy Excitations of a Bose-Einstein Condensate: A Time-Dependent Variational Analysis, *Phys. Rev. Lett.* **77**, 5320 (1996).
 - [57] D. L. Campbell, R. M. Price, A. Putra, A. Valdés-Curiel, D. Trypogeorgos, and I. B. Spielman, Magnetic phases of spin-1 spin-orbit-coupled Bose gases, *Nat. Commun.* **7**, 18983 (2016).
 - [58] X. Luo, L. Wu, J. Chen, Q. Guan, K. Gao, Z.-F. Xu, L. You, R. Wang, Tunable atomic spin-orbit coupling synthesized with a modulating gradient magnetic field, *Sci. Rep.* **6**, 18983 (2016).
 - [59] K. Sun, C. Qu, Y. Xu, Y. Zhang, and C. Zhang, Interacting spin-orbit-coupled spin-1 Bose-Einstein condensates, *Phys. Rev. A* **93**, 023615 (2016).
 - [60] G. Martone, F. Pepe, P. Facchi, S. Pascazio, and S. Stringari, Tricriticalities and Quantum Phases in Spin-Orbit-Coupled Spin-1 Bose Gases, *Phys. Rev. Lett.* **117**, 125301 (2016).
 - [61] Z.-Q. Yu, Phase transitions and elementary excitations in spin-1 Bose gases with Raman-induced spin-orbit coupling, *Phys. Rev. A* **93**, 033648 (2016).
 - [62] X.-W. Luo, K. Sun, and C. Zhang, Spin-tensor-momentum-coupled Bose-Einstein condensates, [arXiv:1705.03920](#).
 - [63] H. Hu, J. Hou, F. Zhang, and C. Zhang, Topological Triply-Degenerate Points Induced by Spin-Tensor-Momentum Couplings, [arXiv:1709.04964](#).